Intermetallics 179 (2025) 108686

Contents lists available at ScienceDirect

Intermetallics

journal homepage: www.elsevier.com/locate/intermet

Interfacial reaction and IMC growth kinetics at the Bi_2Te_3/Ag interface during isothermal aging

Seong-Woo Pak [a,b,*], Hiroaki Tatsumi [a], Jianhao Wang [a], Albert T. Wu [c], Hiroshi Nishikawa [a,**]

[a] Joining and Welding Research Institute, Osaka University, Ibaraki, Osaka, 567-0047, Japan
[b] Graduate School of Engineering, Osaka University, Suita, Osaka, 565-0871, Japan
[c] Department of Chemical and Materials Engineering, National Central University, No. 300, Zhongda Road, Zhongli District, Taoyuan City, 32001, Taiwan

ARTICLE INFO

Keywords:
Intermetallic compound
IMC growth kinetics
Microstructural evolution
Thermoelectric
Ag sintering

ABSTRACT

Bonding materials that can withstand high operating temperatures are essential for increasing the conversion efficiencies of thermoelectric power-generation devices. Sn-based solders commonly used to join thermoelectric materials and electrodes have the disadvantage of limiting the maximum operating temperature to 150 °C because of their low melting point. To overcome this limitation, in the present study, Ag nanoparticle paste with high-temperature stability, low electrical resistivity, high thermal conductivity, and printability was used for bonding a Bi_2Te_3 thermoelectric material and an electroless nickel immersion gold (ENIG)-plated Cu electrode.

We performed isothermal aging at 200 °C from 0 to 1000 h to analyze the microstructural and thickness changes in intermetallic compounds (IMCs). Initially, a heterogeneous distribution of the IMC layers was observed at the bonding interface; over time, the IMC structures became clearly distinct. The IMC thickness increased from ≤3.0 μm (initial) to 45.6 μm in 1000 h, growing by a factor of approximately 15.2. We analyzed the growth kinetics of AgTe and BiTe IMCs. The growth exponent n of the AgTe IMC was found to be 0.3, indicating grain boundary diffusion with grain-growth control, whereas the n value of the BiTe IMC was 0.5, which is consistent with volumetric diffusion-controlled growth. These differences in the growth behavior indicate that different diffusion mechanisms affect the reliability and performance of the bonding interface.

1. Introduction

Energy efficiency and global warming have recently attracted considerable attention. There is an urgent need to reduce energy consumption and carbon emissions [1]. Thermoelectric (TE) materials play an important role in the development of renewable energy [2–4]. They convert waste heat from plants into electricity through the Seebeck effect [5–8]. Another unique property of TE materials is the Peltier effect, which creates a temperature gradient across the material when an electric current passes through it [2]. TE materials such as GeTe [9], PbTe [10], Bi_2Te_3 [11], silicides [12], and Heusler alloys [13] have been studied for use at various operating temperatures.

Many industries generate large amounts of waste heat at low temperatures. It is difficult to use low-temperature waste heat in the temperature range below 200 °C. TE materials convert heat into power using temperature gradients and are effective for harvesting waste heat [14]. TE power-generation devices based on TE materials have no mechanically moving parts, are compact, and remain silent during operation [15]. TE technology has attracted the attention of many researchers for the conversion of industrial waste heat into renewable energy.

Generally, TE materials are classified according to the temperature range in which they are used [4]. For example, Bi_2Te_3 exhibits better TE performance at operating temperatures below 200 °C [16,17]. TE generators are manufactured by arranging p- and n-type TE materials in a π-shaped pattern, combining them with Cu electrodes, and inserting them between two insulating substrates with high thermal conductivity. Heat flows from the bottom of the substrate to the top, organizing all the TE elements thermally in parallel and electrically in series [18]. Owing to these advantages, TE devices are used in various applications, such as remote power supplies (radioisotope TE generators), automobiles, temperature sensors, control devices, and wearable devices [19,20]. The reliability of TE devices is severely limited by the figure of merit (zT) of

* Corresponding author. Joining and Welding Research Institute, Osaka University, Ibaraki, Osaka, 567-0047, Japan.
** Corresponding author.
E-mail addresses: u358637i@ecs.osaka-u.ac.jp (S.-W. Pak), nisikawa.jwri@osaka-u.ac.jp (H. Nishikawa).

https://doi.org/10.1016/j.intermet.2025.108686
Received 21 August 2024; Received in revised form 20 January 2025; Accepted 26 January 2025
Available online 31 January 2025

the TE material, as well as the bonded interface between the TE material and electrodes [21,22]. To develop a TE device with a reliable bonding interface, bonding technology suitable for heat-sensitive TE materials that supports both low-temperature bonding and high-temperature operation is required. However, these joints suffer from problems such as poor bonding, severe mismatch in the coefficient of thermal expansion, and brittle intermetallic compound (IMC) formation [14]. In particular, the rapid growth of IMCs between the TE material and the electrodes must be prevented. Typically, in the production of TE devices, a bond between the TE materials and conductive electrodes is formed through soldering [23,24]. Sn-based solders are commonly used as bonding materials in electronics devices [25–27] and some soldering processes are applied [28,29]. The Sn-based solders can easily react with Bi_2Te_3 and form a brittle SnTe IMC at the interface, which reduces the reliability of the joint, degrading the performance of the TE device [30–33]. Chen and Chiu reported that the SnTe IMC grew rapidly when Sn reacted with pure Te [34]. Thus, excessive growth of the IMC formed at the interface between the TE and bonding materials affects the performance of the solder joint and the reliability of the TE device. Understanding the growth kinetics of IMC is essential for developing robust and reliable TE devices. As an alternative to Sn-based solders, a sintering method using an Ag nanoparticle paste has been developed to bond Bi_2Te_3 and a conductive electrode for providing a more stable interface.

The main advantages of Ag sintering technology are the low electrical resistivity (i.e., 2.5 to 10 μ·Ω·cm [35]) of the sintered Ag joints and the low-temperature bonding process that occurs at approximately 250 °C [36]. Sintered Ag joints have demonstrated high temperature stability and high thermal and electrical conductivities [37,38]. Even when Ag nanoparticles are used, an IMC is created between the Bi_2Te_3 TE material and sintered Ag owing to the reaction among Bi, Te, and Ag [39]. Therefore, interfacial reaction and IMC growth behavior at the sintered interface are important. However, studies on the IMC formation and growth at the interface using Ag nanoparticle pastes are lacking.

To investigate the growth behavior of the IMC at the interface using Ag nanoparticle paste, aging experiments were conducted in this study under various aging times and constant-temperature conditions. We analyzed the diffusion behavior of the elements between the Bi_2Te_3 alloy and sintered Ag layer and investigated the IMC formation process. The results of this study indicate that low-temperature bonding using Ag nanoparticle paste is a reliable method for TE-device manufacturing. This study contributes to the understanding of IMC growth and interfacial reactions at the Bi_2Te_3/Ag interface. By analyzing the behavior and evolution of IMCs, we provide information that can improve low-temperature bonding technologies and enhance the reliability and performance of TE devices.

2. Experimental procedures

A Ru-doped n-type Bi_2Te_3 alloy (Toshima Manufacturing Co., Ltd., Japan) was used in this study. The Bi_2Te_3 sintered body was cut into 3 mm × 3 mm × 1 mm pieces using an IsoMet low-speed precision cutter (Buehler Ltd., USA). The surface of Bi_2Te_3 substrate was carefully polished using 0.1- and 1-μm Al_2O_3 suspensions to remove impurities and reduce its roughness, and it was then successively cleaned with ethyl alcohol and distilled water in an ultrasonic bath.

Ag nanoparticle paste (SR9200, Bando Chemical Industries, Ltd., Japan) was used as the bonding material. Bi_2Te_3 as the chip and an ENIG-plated Cu disk as the conductive electrode were bonded. ENIG-plated Cu disks with a height of 5 mm and diameter of 10 mm were used in this study to ensure a smooth reaction with the Ag nanoparticle paste. At this time, the thicknesses of the Ni-P and Au plating layers were 5 and 0.1 μm, respectively. A detailed structural schematic of the Bi_2Te_3/Ag/ENIG-Cu bonded sample is shown in Fig. 1(a)–(c).

Ag nanoparticle paste was printed onto ENIG-plated Cu disks through a 100-μm-thick stencil pattern mask. To vaporize the solvent and remove voids in the Ag nanoparticle paste, pre-heating was performed using a hot plate at 85 °C for 480 s. This was followed by bonding at a peak temperature of 250 °C for 600 s to ensure successful bonding of

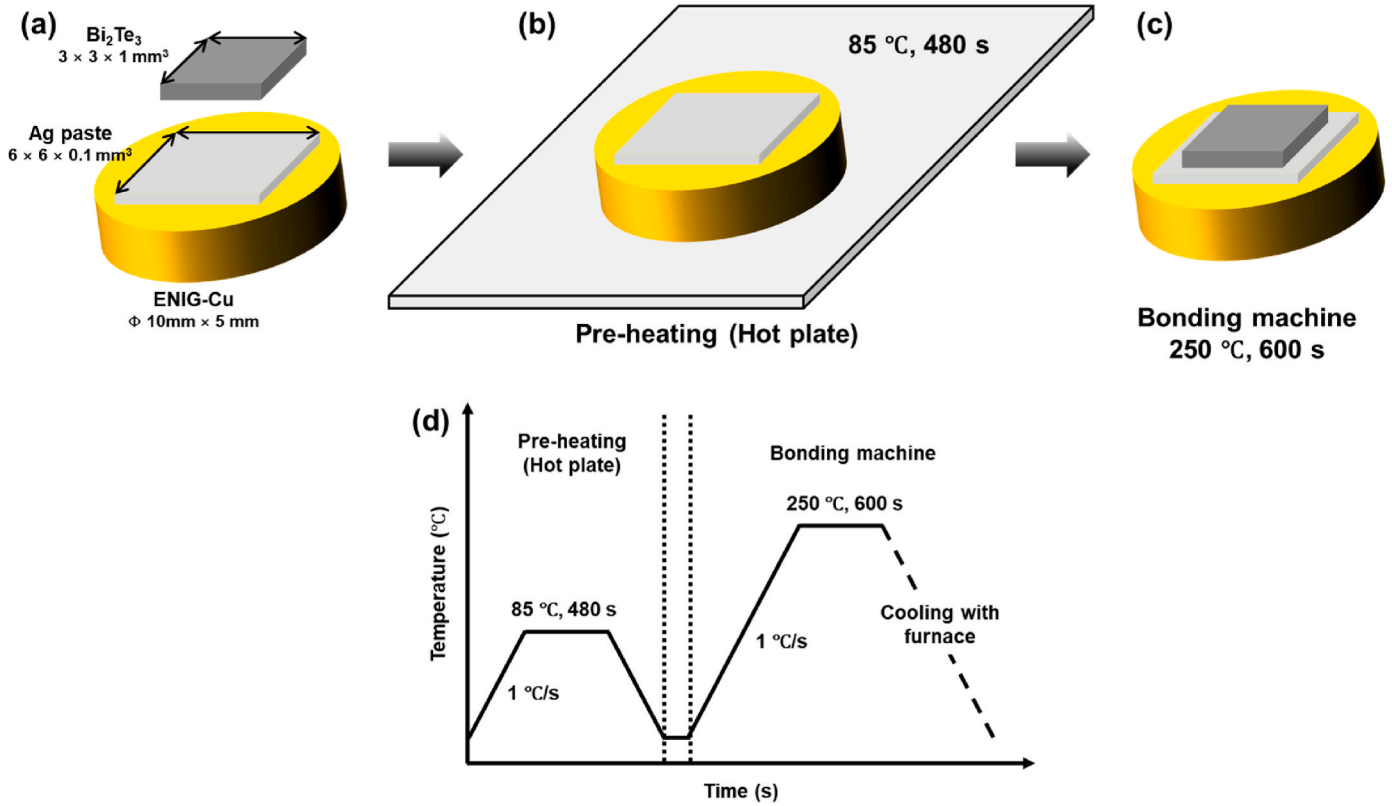

Fig. 1. (a)–(c) Schematic of the experimental procedure and (d) sintering process.

the Bi_2Te_3/Ag/ENIG-Cu samples. All the bonding processes were performed under pressureless conditions in an air atmosphere. The heating profile is shown in Fig. 1(d). The bonding was performed using a sintering machine (RB-100D; Ayumi Industry Co., Ltd, Japan).

Bonded samples prepared for thermal aging were stored in an oven at 200 °C for 0, 50, 100, 200, 500, or 1000 h. After the thermal aging, they were removed from the oven and cooled to room temperature in air. Subsequently, the bonded samples were immersed in epoxy resin and polished using #2000 SiC paper and a 1-μm Al_2O_3 suspension, and the IMC growth of the joint was observed over time at a constant heat-treatment temperature.

Samples for micro-X-ray diffraction (XRD) analysis were prepared using the diagonal grinding method. For expanding the thin IMC layer to a larger area, a support material was placed at the bottom of the bonded sample to set the desired angle of inclination. The sample immersed in epoxy resin was delicately polished in the vertical direction relative to the support material, and the IMC layer, which was initially as thin as ≤10 μm, was expanded to a maximum thickness of 100 μm. After sampling, a micro-X-ray diffractometer (D8 Discover, Bruker, United States) was used to identify the IMC phase formed at the bonding interface between the Bi_2Te_3 and sintered Ag. XRD patterns were collected using the micro-X-ray diffractometer with Co Ka radiation at room temperature in the 2θ range of 20°–80°. The conditions were as follows: 45 kV and 100 mA; step size, 0.02°; scan rate, 4°/min; incident angle, 0.2°.

The cross-section of each sample was examined using backscattered electron (BSE) images via a scanning electron microscopy (SEM; SU8220, Hitachi, Japan) to analyze the interfacial IMC. The chemical compositions of the phases were determined via energy-dispersive X-ray spectroscopy (EDS).

To determine the thickness of the IMCs, a quantitative metallography technique was used [40]. The average thickness of the interfacial IMC was calculated by measuring the area of the IMC formed at the interface using an image analysis program and dividing it by the total length of the image. To increase the accuracy, the average thickness was obtained from five random locations. The growth behavior of the IMC was evaluated by quantifying the change in the IMC thickness according to the isothermal aging time.

3. Results and discussion

3.1. Initial interfacial microstructure

The structure of the as-bonded Bi_2Te_3/Ag interface was evaluated via cross-sectional observations. Fig. 2 shows a cross-sectional BSE image of the as-bonded interface between the Bi_2Te_3 and sintered Ag layer. The reaction between Bi_2Te_3 and Ag confirmed that a thin reaction layer was formed at the interface, with an average thickness of approximately 3.0 μm. The reaction layer contained two phases with different color contrasts that were homogeneously mixed. Point analysis by EDS was performed to investigate the composition of the two phases observed in the reaction layer, as shown in Fig. 2. A1 consisted of 57.8 at.% Ag, 40.6 at.% Te, and 1.6 at.% Bi, while A2 consisted of 53.2 at.% Bi, 45.3 at.% Te, and 1.5 at.% Ag.

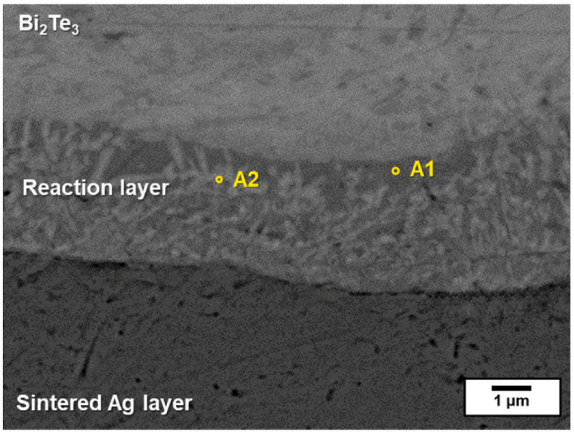

Fig. 2. Cross-sectional BSE image of the reaction layer at the Bi_2Te_3/Ag bonding interface under the as-bonded condition.

As shown in Fig. 3, the elemental mapping analysis was conducted by EDS to analyze the microstructure and phases within the reaction layer at the Bi_2Te_3/Ag bonding interface under the as-bonded condition. Fig. 3 (a) shows a BSE image of the reaction layer at the interface, where two phases appear as regions with distinct color contrasts. The elemental mappings for Ag, Te, and Bi in Fig. 3(b)–(d) reveal regions with distinct elemental distributions, indicating the formation of separate phases within the reaction layer. According to the EDS results, Ag, Te, and Bi were observed to be mixed within the reaction layer, indicating that the three elements diffused into each other.

XRD analysis was used to identify the phases in the IMC layer at the bonding interface, as shown in Fig. 4. Peaks corresponding to each phase were identified using JCPDS cards for Ag (No. 01-071-4613), Bi_2Te_3 (No. 00-002-0524), BiTe (No. 00-042-1268), and AgTe (No. 00-016-0412). The XRD and EDS results indicated that Ag and Bi_2Te_3 were present in the sintered Ag layer and Bi_2Te_3 chip, respectively. According to the XRD results, the IMC layer shown in Fig. 3 consisted of BiTe and AgTe phases.

3.2. Interfacial microstructure after thermal aging for 50 h

The structure of the Bi_2Te_3/Ag bonding interface aged at 200 °C for 50 h was evaluated through cross-sectional observations. Fig. 5 shows a cross-sectional BSE image of the interface between the Bi_2Te_3 and the sintered Ag layer after 50 h of aging. Through the solid-state reaction between Bi_2Te_3 and Ag, a thick multilayer IMC was formed at the interface. The multilayer IMC was composed of three layers: A, B, and C, from the Bi_2Te_3 chip side to the sintered Ag layer side. Layers A and B were flat and dense, respectively. Layer C was thicker than layers A and B and comprised a mixture of dark and bright regions. After aging for 50 h, the average thickness of the overall IMC was increased from 3.0 to 12.2 μm. Additionally, the average thicknesses of layers A, B, and C were approximately 2.7, 1.6, and 7.8 μm, respectively.

The IMC compositions after 50 h of aging were determined using EDS, as shown in Table 1. Regions B1 and B5 shown in Fig. 5 represent the Bi_2Te_3 chip and sintered Ag layer, respectively. Region B2 within layer A showed a composition of 56.5 at.% Ag, 39.4 at.% Te, and 3.9 at.% Bi, indicating a high contents of Ag and Te, i.e., an Ag-Te IMC. Region B3 within layer B showed a composition of 52.6 at.% Bi, 45.3 at.% Te, and 2.0 at.% Ag, indicating a high contents of Bi and Te, i.e., a Bi-Te IMC. The resolution of the EDS analysis was insufficient to distinguish the mixed dark and bright regions in the BSE image; however, region B4 within layer C showed a composition of 56.1 at.% Bi, 25.3 at.% Ag, and 18.6 at.% Te.

The distributions of Ag, Te, and Bi at the Bi_2Te_3/Ag bonding interface as observed via EDS are shown in Fig. 6. Fig. 6(a) shows a BSE image of the IMC structure at the interface after aging at 200 °C for 50 h. First, the layered IMC structure with dark gray and light gray color phases were observed on the Bi_2Te_3 side. Then, an IMC region with two phases with distinct color contrast was observed below the layered IMC structure. Fig. 6(b) shows the distribution of Ag in the sintered Ag layer as well as in the upper and part of middle regions of the IMC area. This distribution indicates that sintered Ag layer react with the Bi_2Te_3 chip during aging. Fig. 6(c) shows the distribution of Te, showing that it is evenly distributed across the Bi_2Te_3 chip and the IMC area. Fig. 6(d) shows the distribution of Bi, which is distributed within the Bi_2Te_3 chip and part of the IMC area.

Fig. 7 shows that the XRD analysis was used to identify the phases in

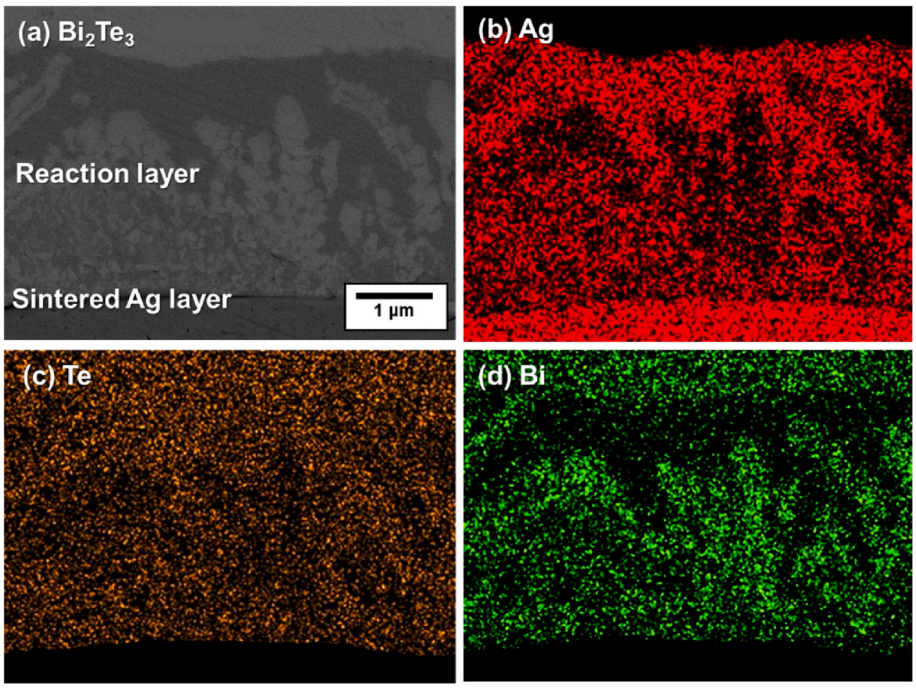

Fig. 3. Elemental distribution of Ag, Te, and Bi in the reaction layer at the Bi_2Te_3/Ag bonding interface investigated by EDS-Mapping under the as-bonded condition. (a) BSE image. (b)–(d) Elemental mapping for Ag, Te, and Bi, respectively.

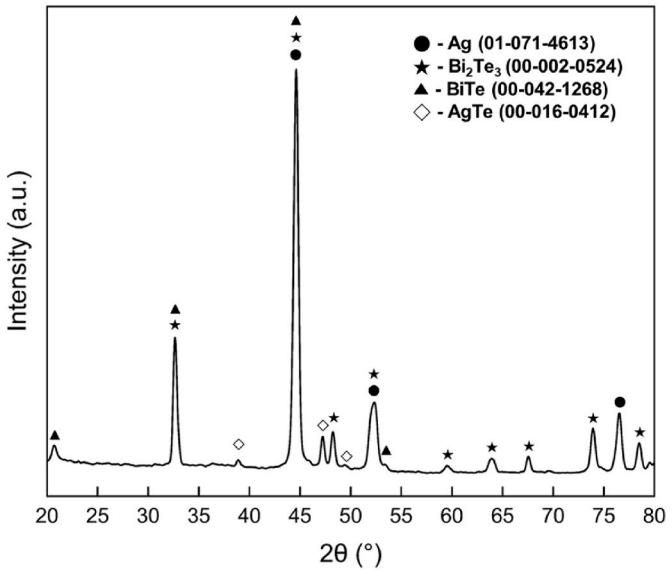

Fig. 4. XRD pattern of the IMC at the Bi_2Te_3/Ag bonding interface under the as-bonded condition.

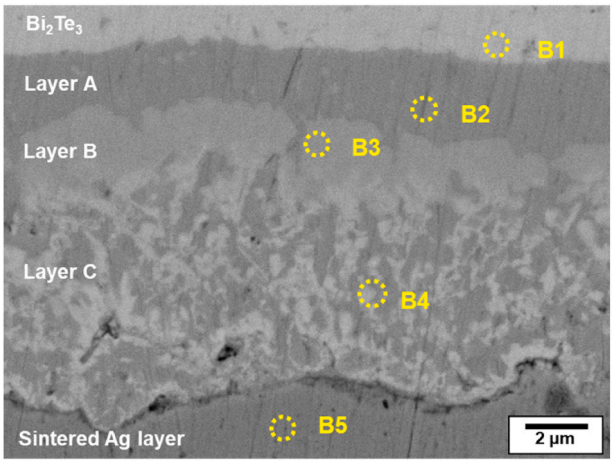

Fig. 5. Cross-sectional BSE image of the IMC microstructure at the Bi_2Te_3/Ag bonding interface after aging at 200 °C for 50 h.

the IMC layer at the Bi_2Te_3/Ag bonding interface after aging at 200 °C for 50 h. Bi and Cu peaks are observed in addition to the Ag, Bi_2Te_3, BiTe, and AgTe peaks observed for the as-bonded sample, which were compared with the Ag (No. 01-071-4613), Bi_2Te_3 (No. 00-002-0524), BiTe (No. 00-042-1268), AgTe (No. 00-016-0412), Bi (No. 01-070-5673), and Cu (No. 00-004-0836) cards of the JCPDS database to confirm excellent crystallinity. These XRD results are consistent with the EDS elemental analysis results, as detailed in Table 1. The EDS analysis indicated that layer A contained 56.5 at.% Ag and 39.4 at.% Te, and XRD pattern confirmed it to be an AgTe phase. Likewise, layer B contained 52.6 at.% Bi and 45.3 at.% Te, and XRD pattern confirmed it to be a BiTe phase.

Table 1
Composition of the IMC formed at the Bi_2Te_3/Ag bonding interface after aging at 200 °C for 50 h.

Region	Main elements (at.%)			Expected phase
	Ag	Te	Bi	
B1	0.41	59.00	40.59	Bi_2Te_3
B2	56.53	39.46	3.92	AgTe
B3	2.06	45.32	52.62	BiTe
B4	25.31	18.57	56.12	Mixture of AgTe and BiTe
B5	100.00	–	–	Sintered Ag layer

No peaks corresponding to the Ag-Bi-Te ternary phase were detected in the XRD pattern. Therefore, layer C may have been a mixture of AgTe and BiTe. The Bi peak identified in the XRD analysis indicates that some Bi, which did not participate in the interdiffusion reaction between

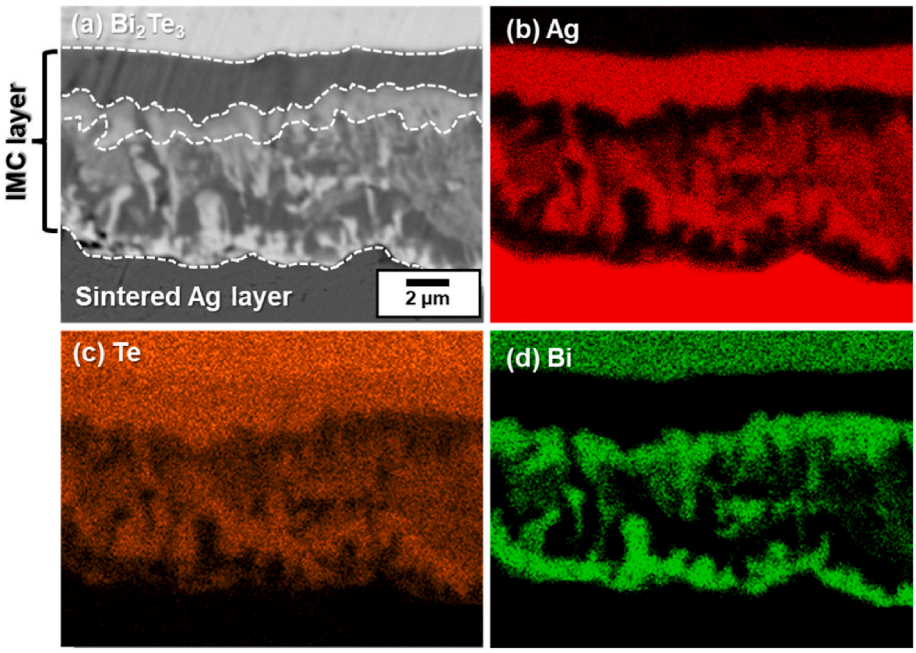

Fig. 6. Elemental distribution of Ag, Te, and Bi in the IMC layer at the Bi_2Te_3/Ag bonding interface investigated by EDS-Mapping after aging at 200 °C for 50 h. (a) BSE image. (b)–(d) Elemental mapping for Ag, Te, and Bi, respectively.

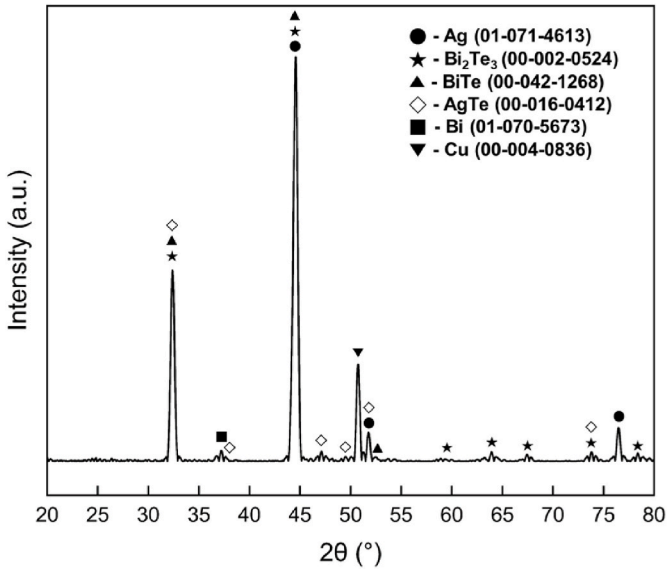

Fig. 7. XRD pattern of the IMC of Bi_2Te_3/Ag bonding interface after aging at 200 °C for 50 h.

Bi_2Te_3 and Ag during aging, remained in its pure form rather than forming a compound. Additionally, the Cu peak observed in the XRD results could be an artifact of the XRD sampling process.

3.3. Interfacial microstructure after thermal aging from 100 to 1000 h

The Bi_2Te_3/Ag bonding interface was subjected to aging treatment at 200 °C for 100, 200, and 500 h to observe the changes in the IMC microstructure, as shown in the BSE images in Fig. 8(a)–(c). The microstructural morphology at the Bi_2Te_3/Ag bonding interface remained similar to that of the sample aged for 50 h. As the aging time increased, the IMC grew while maintaining a constant layered structure, and its thickness increased. The IMC aged for 100 h had an average thickness of 16.6 μm and was relatively thin and irregularly shaped. As the aging time increased to 200 and 500 h, the average thickness of the IMC increased to 19.7 and 29.0 μm, respectively. This microstructural evolution suggests that the IMC continued to grow with increasing aging time, becoming thicker and flatter.

Fig. 9 presents a cross-sectional BSE images of the IMC microstructure at the Bi_2Te_3/Ag bonding interface after aging for 1000 h. As shown in Fig. 9(a), the IMC microstructure retained a uniform layered structure, similar to the samples aged for 50–500 h. After aging for 1000 h, the IMC thickness increased to an average of 45.6 μm.

Fig. 9(b) presents a high-magnification BSE image of IMC layer C. The IMC composition after aging for 1000 h was determined via EDS analysis, and the results are presented in Table 2. The continuously formed layers A and B were identified as AgTe and BiTe phases, respectively, based on the EDS analysis of regions C1 and C2. Additionally, region C3a in IMC layer C was determined to have a composition of 57.5 at.% Bi, 22.9 at.% Te, and 19.5 at.% Ag. Because of the resolution limit of EDS, Ag elements from adjacent areas were detected, which led to the inclusion of Ag in the results. Furthermore, region C3b in IMC layer C was determined to have a composition of 59.7 at.% Ag, 35.9 at.% Te, and 4.2 at.% Bi. These results confirmed that the IMC microstructure, even after aging for 1000 h, was similar to that observed under the aging conditions from 50 to 500 h. It was confirmed that IMC layer C was composed of a mixture of AgTe and BiTe phases.

3.4. Aging effects on IMC formation

The aging effect on the IMC microstructure formation at the Bi_2Te_3/Ag bonding interface was investigated. The composition of this unique multilayer structure was confirmed through EDS and XRD analysis. Fig. 10 presents a schematic of the formation of the interfacial microstructure. Fig. 10(a) shows the initial arrangement of each element and the starting point of the Bi_2Te_3/Ag bonding process. Fig. 10(b) shows the IMC layer in the as-bonded condition. A thin IMC layer was formed at the interface between Bi_2Te_3 and Ag, with a thickness of $\leq$3 μm. The IMC microstructure consisted of a mixture of AgTe and BiTe, which was formed by the interdiffusion reaction at the interface. This indicates that the IMC begins to form through a solid-state diffusion process initiated by an interdiffusion reaction involving Ag, Te, and Bi.

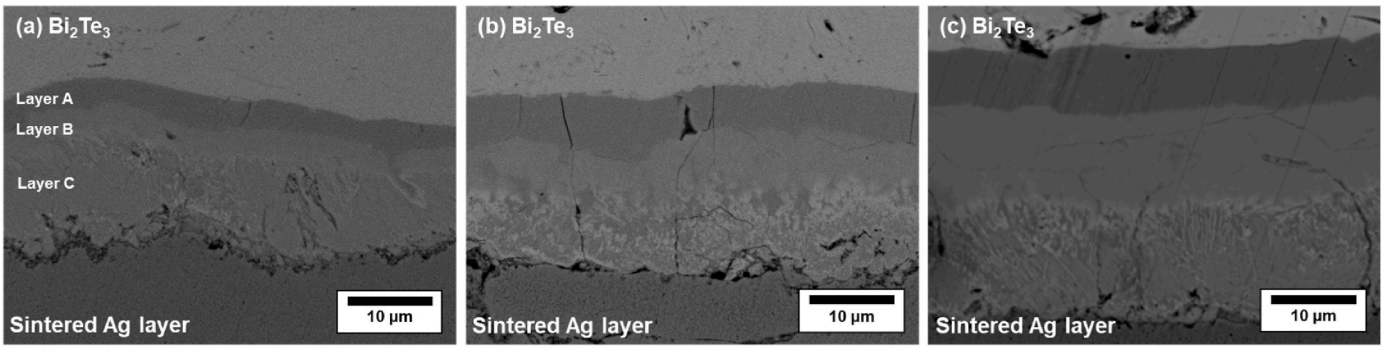

Fig. 8. Cross-sectional BSE images of the IMC microstructure at the Bi_2Te_3/Ag bonding interface after aging at 200 °C for (a) 100 h, (b) 200 h, and (c) 500 h, under different conditions.

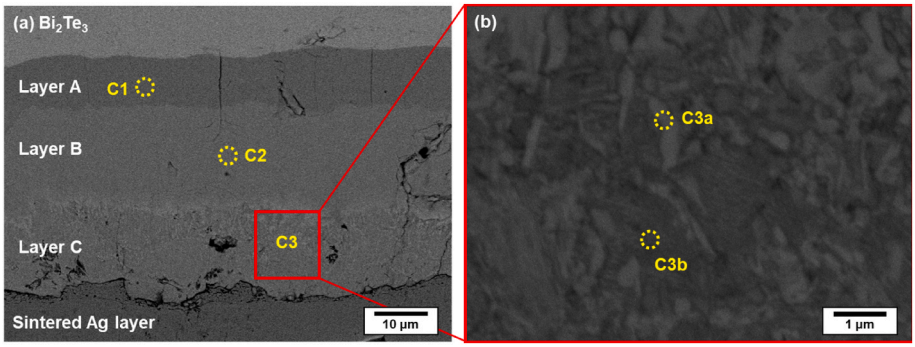

Fig. 9. Cross-sectional BSE images and EDS point analysis of the IMC microstructure at the Bi_2Te_3/Ag bonding interface (a) after aging at 200 °C for 1000 h and (b) high-magnification image of IMC layer C.

Table 2
IMC composition formed at the Bi_2Te_3/Ag bonding interface after aging at 200 °C for 1000 h.

Region	Main elements (at.%)			Expected phase
	Ag	Te	Bi	
C1	57.87	39.68	2.45	AgTe
C2	5.41	40.46	54.13	BiTe
C3a	19.51	22.96	57.53	BiTe
C3b	59.77	35.96	4.27	AgTe

The IMC formation process is described by Eq. (1).

$$Bi_2Te_3 + Ag \rightarrow AgTe + 2BiTe \quad (1)$$

This reaction is based on the interdiffusion of Bi_2Te_3 and Ag, where AgTe and BiTe IMCs are formed as reaction products.

Fig. 10(c) shows that during the aging, the IMC microstructure became more distinctly divided into three layers, indicating an increase in the overall IMC thickness. In the early stage of aging, the overall thickness of the IMC increased, and a continuous layer was formed at the interface between the Bi_2Te_3 and sintered Ag layers. This multilayer structure consisted of an AgTe IMC, a BiTe IMC, and mixed AgTe and BiTe IMC layers. It was formed by interdiffusion and rearrangement at the interface. Fig. 10(d) shows that the IMC microstructure finally formed at the Bi_2Te_3/Ag bonding interface in the later stage of the long-term aging treatment. Even in the later stage of aging, the thickness of the IMC continued to increase, while the morphology was maintained.

3.5. Formation mechanism of the mixed AgTe and BiTe layer

At the interface between the Bi_2Te_3 and sintered Ag layer, the mixed AgTe and BiTe IMC layer was formed in the as-bonded condition and the multilayer structure was formed during the aging. The formation mechanism of the mixed AgTe and BiTe IMC layer observed at the Bi_2Te_3/Ag bonding interface was investigated by analyzing the thermodynamic properties of these layers. Table 3 summarizes the standard Gibbs free energy change (ΔG°), enthalpy change (ΔH°), and entropy change (ΔS°) for each compound, as obtained in previous studies [41, 42].

For both AgTe and BiTe, the changes in the Gibbs free energy, enthalpy, and entropy play a critical role in their formation behaviors. The values of ΔG°, ΔH°, and ΔS° were −20.41, −15.98, and 107.1 J/K·mol for AgTe, respectively, and −29.3, −45.1, and 53.0 J/K·mol for BiTe, respectively. The more negative Gibbs free energy for BiTe suggests a higher thermodynamic stability during its formation compared to AgTe. In addition, the enthalpy of formation ($\Delta_f H^\circ$) for BiTe (−45.1 ± 1.3 kJ/mol) is significantly lower than that of AgTe (−15.98 ± 0.06 kJ/mol). This lower enthalpy further reinforces the thermodynamic stability of BiTe, allowing it to become a more prominent phase within the structure during extended aging. This thermodynamic stability combined with the interdiffusion reaction contributes to formation of the mixed AgTe and BiTe layer.

3.6. Growth behavior of the AgTe and BiTe intermetallic layer

The growth behavior of the AgTe and BiTe IMC formed at the Bi_2Te_3/Ag bonding interface was investigated. The thickness changes of the IMC and the growth rates during aging were analyzed to investigate the IMC growth mechanisms.

Fig. 11 shows a visual representation of the average thickness change of the IMC formed at the Bi_2Te_3/Ag bonding interface during aging at 200 °C for various times. As the aging time increased, the total IMC thickness at the Bi_2Te_3/Ag bonding interface increased. To analyze the growth rate of the IMC formed at the Bi_2Te_3/Ag bonding interface with

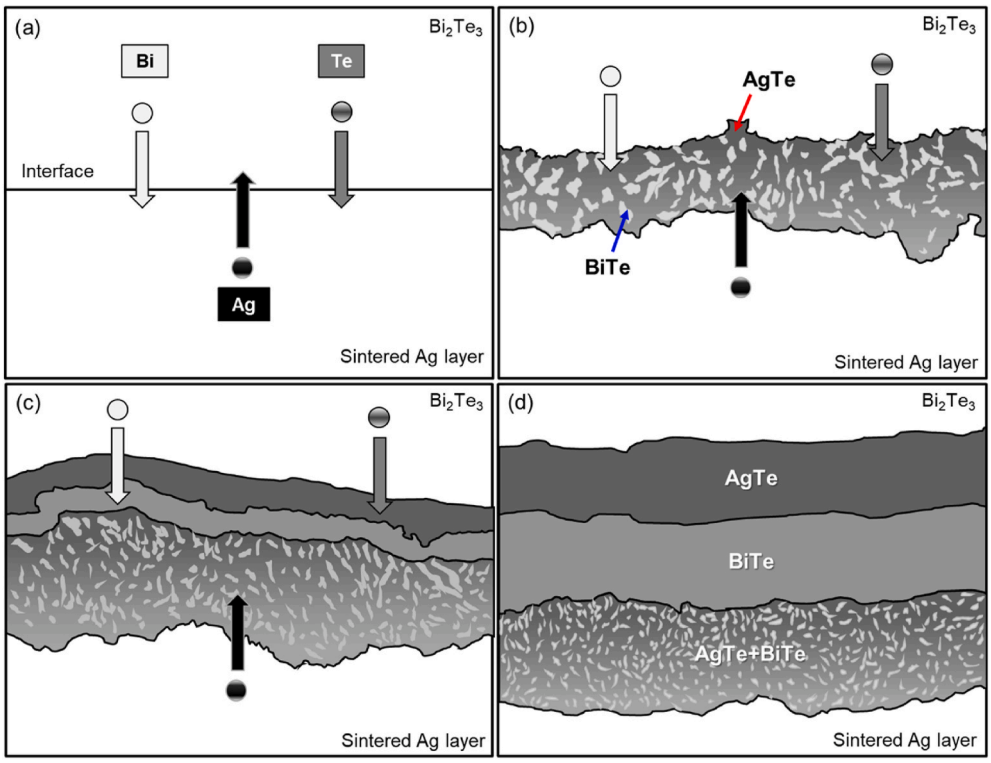

Fig. 10. Schematic of the IMC formation process at the Bi_2Te_3/Ag bonding interface: (a) initial stage; (b) as-bonded condition; (c) 50–100 h; (d) 200–1000 h.

Table 3
Standard thermodynamic properties of compounds in the Ag–Te and Bi-Te system at 298.15 K and 1 bar.

Compound	$\Delta_f G°$ (kJ mol^{-1})	$\Delta_f H°$ (kJ mol^{-1})	$S°$ (J K^{-1} mol^{-1})	Reference
AgTe	−20.41 ± 0.06	−15.98 ± 0.06	107.1 ± 0.9	[41]
BiTe	−29.3 ± 2.4	−45.1 ± 1.3	53.0 ± 6.0	[42]

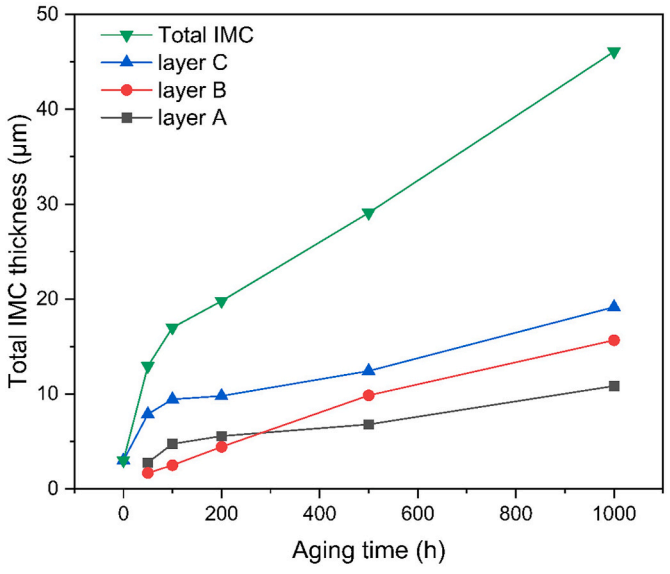

Fig. 11. Average thicknesses of IMCs as a function of the aging time.

respect to the aging time, the thickness of each IMC layer was measured. As the aging time increased from 0 to 1000 h, the thicknesses of the AgTe IMC, BiTe IMC, and mixed AgTe and BiTe IMC aged samples were measured to be 10.8, 15.6, and 19.1 μm, respectively. The total IMC thickness increased from an initial 3.0–45.6 μm, i.e., by a factor of approximately 15.2, as aging progressed.

In this study, we analyzed the growth behaviors of AgTe and BiTe IMCs. However, the growth of the IMC layer C region, where the AgTe and BiTe IMCs were randomly mixed, is not discussed, because of its complex interdiffusion.

Fig. 12 shows the logarithm of the AgTe and BiTe IMC layer thicknesses as a function of the logarithm of the aging time. Here, the

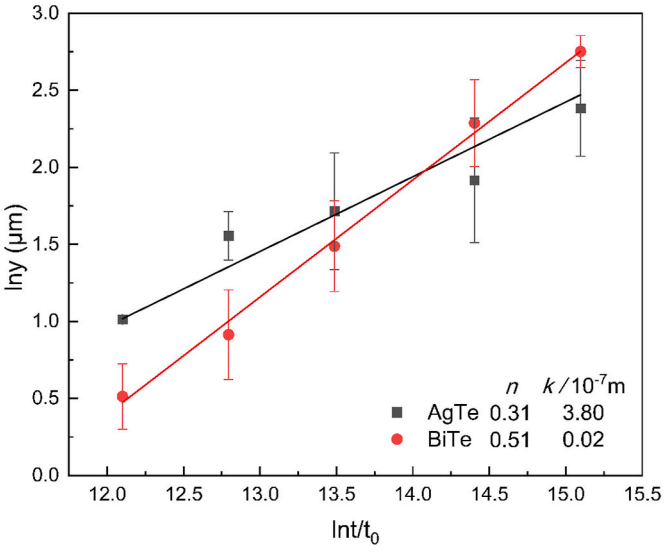

Fig. 12. Logarithmic plot of AgTe and BiTe IMC layer thickness as a function of aging time at 200 °C, represented by squares and circles, respectively.

ordinate and abscissa axes indicate the natural logarithms of y and t, respectively. As shown, the thickness of the IMC layer (μm), ln(y), increases with the aging time, ln(t). This implies that y can be mathematically expressed as a power function of t using Eq. (2) [43]:

$$\ln(y) = \ln(k) + n \bullet \ln(t / t_0), \quad (2)$$

where t_0 represents the unit time (1 s), which is introduced to ensure that t/t_0 is dimensionless. The proportionality coefficient k has the same dimensions as that for the thickness, and n is the growth exponent, which is dimensionless. Using the experimental data points in Fig. 12, the values of k and n were estimated by applying the least-squares method, as indicated by the solid lines.

In general, if the IMC growth mechanism obeys the diffusion-controlled process, the n value is equal to 0.5. This value is obtained for layer growth controlled by volume diffusion, provided no grain growth occurs within the intermetallic layer. However, if grain growth occurs, the presence of grain boundaries reduces the effective diffusion path, resulting in an n value less than 0.5, indicating grain boundary diffusion control [44]. Researchers have reported similar rate-controlling processes for solid-state reactive diffusion in various metal systems, such as Ta/Cu-Sn-Ti and Cu/Zn [45,46]. Furthermore, n can equal 0.25 if grain growth follows the parabolic law, where the mean grain size increases in proportion to the square root of the aging time [47,48].

In this study, the n value of the AgTe IMC was 0.3, suggesting layer growth was predominantly controlled by grain boundary diffusion with grain growth at 200 °C. Conversely, the n value of the BiTe IMC was 0.5, consistent with volume diffusion-controlled growth. As grain growth occurs in the AgTe IMC, the decreasing fraction of the grain boundaries reduces the effective diffusion coefficient, decelerating layer growth, and resulting in an n value below 0.5. The observed growth behavior reflects distinct diffusion pathways. AgTe IMC grows through grain boundary diffusion with grain growth, while BiTe IMC grows through volume diffusion. This difference corresponds to the measured n values of 0.3 and 0.5, respectively. These findings are important for understanding the reliability and performance of IMC growth and its impact on bonding interfaces in practical applications.

4. Conclusion

In this study, the microstructural changes and growth behaviors of IMCs formed at the Bi_2Te_3/Ag bonding interface were investigated through a series of aging treatments at 200 °C. The initial interface exhibited a thin IMC layer consisting of AgTe and BiTe phases. As the aging progressed, the IMC layer evolved into a multilayer structure with distinct AgTe and BiTe layers and a mixed AgTe and BiTe layer. The thickness of the IMC layer increased significantly as the aging time increased, from an initial 3.0 μm–45.6 μm after 1000 h.

The growth kinetics of the IMC layers were characterized by analyzing the growth exponent n. For the AgTe IMC, the n value was 0.3, indicating that its growth was predominantly controlled by grain boundary diffusion. In contrast, for the BiTe IMC, the n value of was 0.5, indicating that its growth was controlled by volumetric diffusion.

CRediT authorship contribution statement

Seong-Woo Pak: Writing – review & editing, Writing – original draft, Methodology, Investigation, Conceptualization. **Hiroaki Tatsumi:** Writing – review & editing, Formal analysis. **Jianhao Wang:** Investigation. **Albert T. Wu:** Validation. **Hiroshi Nishikawa:** Writing – review & editing, Supervision.

Declaration of competing interest

The authors declare that they have no known competing financial interests or personal relationships that could have appeared to influence the work reported in this paper.

Acknowledgements

This research was financially supported by the OU Master Plan Implementation Project promoted under Osaka University. This work was also supported by the Ministry of Trade, Industry, and Energy (MOTIE) of Korea under the Fostering Global Talents for Innovative Growth Program [P0008750], supervised by the Korea Institute for Advancement of Technology (KIAT).

Appendix A. Supplementary data

Supplementary data to this article can be found online at https://doi.org/10.1016/j.intermet.2025.108686.

Data availability

Data will be made available on request.

References

[1] P. Taylor, Energy Technology Perspectives, vol. 692, International Energy Agency, 2010.
[2] D. Rowe, General principles and basic considerations. Thermoelectrics Handbook, 2005.
[3] G. Chen, M.S. Dresselhaus, G. Dresselhaus, J.P. Fleurial, T. Caillat, Recent developments in thermoelectric materials, Int. Mater. Rev. 48 (1) (2003) 45–66.
[4] G.J. Snyder, Application of the compatibility factor to the design of segmented and cascaded thermoelectric generators, Appl. Phys. Lett. 84 (13) (2004) 2436–2438.
[5] G.G. Yadav, J.A. Susoreny, G. Zhang, H. Yang, Y. Wu, Nanostructure-based thermoelectric conversion: an insight into the feasibility and sustainability for large-scale deployment, Nanoscale 3 (9) (2011) 3555–3562.
[6] G.J. Snyder, E.S. Toberer, Complex thermoelectric materials, Nat. Mater. 7 (2) (2008) 105–114.
[7] J. Yang, T. Caillat, Thermoelectric materials for space and automotive power generation, MRS Bull. 31 (3) (2006) 224–229.
[8] L.E. Bell, Cooling, heating, generating power, and recovering waste heat with thermoelectric systems, Science 321 (5895) (2008) 1457–1461.
[9] J. Youn, J. Ryu, H. Kim, S.K. Kihoi, I.S. Son, S.E. Chun, H.S. Lee, Low thermal conductivity in GeTe-based thermoelectric materials with additional activated carbon, Appl. Phys. Lett. 118 (5) (2021).
[10] D. Ben-Ayoun, Y. Sadia, Y. Gelbstein, High temperature thermoelectric properties evolution of Pb1-xSnxTe based alloys, J. Alloys Compd. 722 (2017) 33–38.
[11] O. Meroz, D. Ben-Ayoun, O. Beeri, Y. Gelbstein, Development of Bi2Te2.4Se0.6 alloy for thermoelectric power generation applications, J. Alloys Compd. 679 (2016) 196–201.
[12] Y. Sadia, N. Madar, I. Kaler, Y. Gelbstein, Thermoelectric properties of the quasi-binary MnSi1.73–FeSi2 system, J. Electron. Mater. 44 (2015) 1637–1643.
[13] J.N. Kahiu, U.S. Shenoy, S.K. Kihoi, H. Kim, S. Yi, D.K. Bhat, H.S. Lee, Optimized electronic performance in half-Heusler Ti-doped NbFeSb materials by stoichiometric tuning at the Fe and Sb sites, J. Alloys Compd. 891 (2022) 162033.
[14] X. Ma, S. Hu, W. Hu, Y. Luo, H. Cheng, Experimental investigation of waste heat recovery of thermoelectric generators with temperature gradient, Int. J. Heat Mass Tran. 185 (2022) 122342.
[15] E. Kanimba, Z. Tian, Modeling of a thermoelectric generator device. Thermoelectrics for Power Generation–A Look at Trends in the Technology, Intech open science| open minds, 2016, pp. 461–479.
[16] M.L. Lwin, P. Dharmaiah, B. Madavali, C.H. Lee, D.W. Shin, G. Song, S.J. Hong, Oxide formation mechanism and its effect on the microstructure and thermoelectric properties of p-type Bi0.5Sb1.5Te3 alloys, Intermetallics 103 (2018) 23–32.
[17] T. Lv, Z. Li, Q. Yang, A. Benton, H. Zheng, G. Xu, Synergistic regulation of electrical-thermal effect leading to an optimized thermoelectric performance in Co doping n-type Bi2 (Te0.97Se0.03) 3, Intermetallics 118 (2020) 106683.
[18] E. Yusufu, T. Sugahara, M. Okajima, S. Nambu, K. Suganuma, Effects of microstructure of Ni barrier on bonding interface diffusion behaviors of Bi–Te-based thermoelectric material, J. Alloys Compd. 817 (2020) 152731.
[19] J. Yan, X. Liao, D. Yan, Y. Chen, Review of micro thermoelectric generator, J. Microelectromech. Syst. 27 (1) (2018) 1–18.
[20] C. Yu, K.T. Chau, Thermoelectric automotive waste heat energy recovery using maximum power point tracking, Energy Convers. Manag. 50 (6) (2009) 1506–1512.
[21] S. Ye, J.D. Hwang, C.M. Chen, Strong anisotropic effects of p-type Bi2Te3 element on the Bi2Te3/Sn interfacial reactions, Metall. Mater. Trans. 46 (2015) 2372–2375.
[22] S.W. Chen, C.Y. Wu, H.J. Wu, W.T. Chiu, Interfacial reactions in Sn/Bi2Te3, Sn/Bi2Se3 and Sn/Bi2(Te1− xSex)3 couples, J. Alloys Compd. 611 (2014) 313–318.

[23] H.X. Mi, M.X. Wu, S. Cao, Z.Y. Huang, L. Han, J. Xu, Effect of solder and barrier layer elements on the thermoelectric properties of Bi0.5Sb1.5Te3, Mater. Res. Express 6 (10) (2019) 106310.
[24] J. Cheng, X. Hu, Q. Li, Influence of Ni and Cu electrodeposits on the interfacial reaction between SAC305 solder and the Bi2(Te,Se)3 thermoelectric material, J. Mater. Sci. Mater. Electron. 30 (2019) 14791–14804.
[25] E.H. Sabbar, H.A. Al-Zubaidi, A.K. Aljumaili, M.H. Al-Jumaili, A.I. Al-Jumaili, H. Alsheakh, Effects of Ag content on microstructure evolution, intermetallic compound (IMC) and mechanical behaviour of SAC solder joints, Microelectron. Reliab. 147 (2023) 115103.
[26] P. Zhang, S. Xue, L. Liu, J. Wang, H. Tatsumi, H. Nishikawa, Study on thermal cycling reliability of epoxy-enhanced SAC305 solder joint, Polymers 16 (18) (2024) 2597.
[27] H.T. Lee, K.C. Huang, Effect of solder-joint geometry on the low-cycle fatigue behavior of Sn-x Ag-0.7 Cu, J. Electron. Mater. 45 (2016) 6102–6112.
[28] X. Hu, H. Xu, W. Chen, X. Jiang, Effects of ultrasonic treatment on mechanical properties and microstructure evolution of the Cu/SAC305 solder joints, J. Manuf. Process. 64 (2021) 648–654.
[29] H. Tatsumi, S. Kaneshita, Y. Kida, Y. Sato, M. Tsukamoto, H. Nishikawa, Highly efficient soldering of Sn-Ag-Cu solder joints using blue laser, J. Manuf. Process. 82 (2022) 700–707.
[30] W.C. Lin, Y.S. Li, A.T. Wu, Study of diffusion barrier for solder/n-type Bi2Te3 and bonding strength for p-and n-type thermoelectric modules, J. Electron. Mater. 47 (2018) 148–154.
[31] T.Y. Lin, C.N. Liao, A.T. Wu, Evaluation of diffusion barrier between lead-free solder systems and thermoelectric materials, J. Electron. Mater. 41 (2012) 153–158.
[32] C.H. Wang, M.H. Li, C.W. Chiu, T.Y. Chang, Kinetic study of solid-state interfacial reactions of p-type (Bi,Sb)2Te3 thermoelectric materials with Sn and Sn–Ag–Cu solders, J. Alloys Compd. 767 (2018) 1133–1140.
[33] C.H. Chuang, Y.C. Lin, C.W. Lin, Intermetallic reactions during the solid-liquid interdiffusion bonding of Bi2Te2. 55Se0. 45 thermoelectric material with Cu electrodes using a Sn interlayer, Metals 6 (4) (2016) 92.
[34] S.W. Chen, C.N. Chiu, Unusual cruciform pattern interfacial reactions in Sn/Te couples, Scripta Mater. 56 (2) (2007) 97–99.
[35] R. Khazaka, L. Mendizabal, D. Henry, Review on joint shear strength of nano-silver paste and its long-term high temperature reliability, J. Electron. Mater. 43 (2014) 2459–2466.
[36] X. Milhet, P. Gadaud, V. Caccuri, D. Bertheau, D. Mellier, M. Gerland, Influence of the porous microstructure on the elastic properties of sintered Ag paste as replacement material for die attachment, J. Electron. Mater. 44 (2015) 3948–3956.
[37] V.R. Manikam, K.Y. Cheong, Die attach materials for high temperature applications: a review, IEEE Trans. Compon. Packag. Manuf. Technol. 1 (4) (2011) 457–478.
[38] Z. Zhang, Sintering of Micro-scale and Nanscale Silver Paste for Power Semiconductor Devices Attachment, 2005.
[39] S. Pak, H. Tatsumi, J. Wang, H. Nishikawa, Interfacial Intermetallic Compounds of Bi2Te 3/Cu joint using SAC305 solder and nano-Ag paste, in: 2023 International Conference on Electronics Packaging (ICEP), IEEE, 2023, April, pp. 199–200.
[40] G.F. Vander Voort, S.R. Lampman, B.R. Sanders, G.J. Anton, C. Polakowski, J. Kinson, W.W. Scott Jr, ASM Handbook, vol. 9, Metallography and microstructures, 2004, 44073-0002.
[41] M.V. Voronin, E.G. Osadchii, E.A. Brichkina, Thermochemical properties of silver tellurides including empressite (AgTe) and phase diagrams for Ag–Te and Ag–Te–O, Phys. Chem. Miner. 44 (2017) 639–653.
[42] M.V. Prokhorenko, M.V. Moroz, P.Y. Demchenko, Measuring the thermodynamic properties of saturated solid solutions in the Ag2Te-Bi-Bi2Te3 system by the electromotive force method, Russ. J. Phys. Chem. A 89 (2015) 1330–1334.
[43] M. Kajihara, Kinetics of solid-state reactive diffusion between Au and Al, Mater. Trans. 52 (4) (2011) 677–684.
[44] A. Furuto, M. Kajihara, Numerical analysis for kinetics of reactive diffusion controlled by boundary and volume diffusion in a hypothetical binary system, Mater. Trans. 49 (2) (2008) 294–303.
[45] Y. Tejima, S. Nakamura, M. Kajihara, Kinetics of reactive diffusion between Ta and Cu–9.3 Sn–0.3 Ti alloy, J. Mater. Sci. 45 (2010) 919–928.
[46] Y. Takamatsu, M. Kajihara, Kinetics of solid-state reactive diffusion in the Cu/Zn system, Mater. Trans. 58 (1) (2017) 16–22.
[47] Y.L. Corcoran, A.H. King, N. de Lanerolle, B. Kim, Grain boundary diffusion and growth of titanium silicide layers on silicon, J. Electron. Mater. 19 (1990) 1177–1183.
[48] R. Abbaschian, R.E. Reed-Hill, Physical Metallurgy Principles, fourth ed., Cengage Learning, 2008.